

Design of sign-reversible Berry phase effect in 2D magneto-valley material

Yue-Tong Han(韩曰通), Yu-Xian Yang(杨宇贤), Ping Li(李萍), and Chang-Wen Zhang(张昌文)

Citation: Chin. Phys. B, 2023, 32 (**9**): 097101. DOI: 10.1088/1674-1056/acd920
Journal homepage: http://cpb.iphy.ac.cn; http://iopscience.iop.org/cpb

What follows is a list of articles you may be interested in

Highly anisotropic Dirac fermion and spin transportproperties in Cu-graphane

Chao Wu(吴超), Lichuan Zhang(张礼川), Lin Xia(夏霖), Dong Hao(郝东), Shiqi Li(李仕琪), Lizhi Zhang(张礼智), Yuee Xie(谢月娥), and Yuanping Chen(陈元平)

Chin. Phys. B, 2023, 32 (**8**): 087104. DOI: 10.1088/1674-1056/accff1

Topological properties of tetratomic Su-Schrieffer-Heeger chains with hierarchical long-range hopping

Guan-Qiang Li(李冠强), Bo-Han Wang(王博涵), Jing-Yu Tang(唐劲羽), Ping Peng(彭娉), and Liang-Wei Dong(董亮伟)

Chin. Phys. B, 2023, 32 (**7**): 077102. DOI: 10.1088/1674-1056/aca7ef

SU(3) spin-orbit coupled fermions in an optical lattice

Xiaofan Zhou(周晓凡), Gang Chen(陈刚), and Suo-Tang Jia(贾锁堂)

Chin. Phys. B, 2022, 31 (**1**): 017102. DOI: 10.1088/1674-1056/ac11dc

First-principles investigation of the valley and electrical properties of carbon-doped α-graphyne-like BN sheet

Bo Chen(陈波), Xiang-Qian Li(李向前), Lin Xue(薛林), Yan Han(韩燕), Zhi Yang(杨致), and Long-Long Zhang(张龙龙)

Chin. Phys. B, 2021, 30 (**5**): 057101. DOI: 10.1088/1674-1056/abddac

Control of topological phase transitions in Dirac semimetal films by exchange fields

Fei Yang(杨菲), Hai-Long Wang(王海龙), Hui Pan(潘晖)

Chin. Phys. B, 2017, 26 (**1**): 017102. DOI: 10.1088/1674-1056/26/1/017102

Design of sign-reversible Berry phase effect in 2D magneto-valley material

Yue-Tong Han(韩曰通)[†], Yu-Xian Yang(杨宇贤)[†], Ping Li(李萍), and Chang-Wen Zhang(张昌文)[‡]

School of Physics and Technology, University of Jinan, Jinan 250022, *China*

(Received 6 December 2022; revised manuscript received 9 May 2023; accepted manuscript online 26 May 2023)

Manipulating sign-reversible Berry phase effects is both fundamentally intriguing and practically appealing for searching for exotic topological quantum states. However, the realization of multiple Berry phases in the magneto-valley lattice is rather challenging due to the complex interactions from spin–orbit coupling (SOC), band topology, and magnetic ordering. Here, taking single-layer spin-valley $RuCl_2$ as an example, we find that sign-reversible Berry phase transitions from ferrovalley (FV) to half-valley semimetal (HVS) to quantum anomalous valley Hall effect (QAVHE) can be achieved *via* tuning electronic correlation effect or biaxial strains. Remarkably, QAVHE phase, which combines both the features of quantum anomalous Hall and anomalous Hall valley effect, is introduced by sign-reversible Berry curvature or band inversion of $d_{xy}/d_{x^2-y^2}$ and d_{z^2} orbitals at only one of the K/K' valleys of single-layer $RuCl_2$. And the boundary of QAVHE phase is the HVS state, which can achieve 100% intrinsically valley polarization. Further, a $k \cdot p$ model unveiled the valley-controllable sign-reversible Berry phase effects. These discoveries establish $RuCl_2$ as a promising candidate to explore exotic quantum states at the confluence of nontrivial topology, electronic correlation, and valley degree of freedom.

Keywords: valley polarization, topological phase transition, half-valley semimetal, quantum anomalous valley Hall effect, first-principles calculations

PACS: 71.15.Mb, 71.15.Dx, 73.43.–f, 73.63.–b **DOI:** 10.1088/1674-1056/acd920

1. Introduction

Valleytronics offers a versatile platform for fundamental and applied research for spintronics materials due to its additional valley degree of freedom, apart from charge and spin.[1–4] Two-dimensional (2D) hexagonal lattices such as transition-metal dichalcogenides (TMD) are promising valley materials to manipulate charge, spin, and valley degrees of freedom.[5–11] In such materials, owing to the breaking of the space-inversion symmetry (P), phenomena associated with valley contrasting feature can be explored such as valley Hall effect (VHE) and valley-controllable optical selection rules.[12,13] Recent advances in valleytronics focus on generating valley polarization by breaking time-inversion symmetry (T) and thus lifting the degeneracy of K/K' valleys.[14] Several approaches have been proposed, like optical pumping,[15–17] magnetic doping,[18–20] magnetic proximity effect,[21–23] and applying an external magnetic field.[24–27] Nevertheless, the intrinsic properties have a higher priority than external tunability so as to reach widespread applications in valley-related physics. Hence, intrinsic valley-related materials hosting spontaneous valley-polarization are most desirable, thanks to its advantages of robustness, power efficiency, and simplicity in operation.

Recently, break-through of the discovery of 2D ferrovalley (FV) materials,[28] such as 2H-VSe_2,[28] VSSe,[29] $LaBr_2$,[30] LaBrI,[31] $GdCl_2$,[32] CeI_2,[33] MXenes,[34] and VSi_2N_4,[35] may lay the foundation for a spin-valley composite paradigm induced by the integrated effects of ferromagnetic (FM) order and spin–orbit coupling (SOC), which could facilitate the observation of anomalous valley Hall effect (AVHE). Furthermore, considering the perspective of potential applications in valleytronics, except for AVHE, the exploration for magneto-valley materials with valley-related multiple Hall effect (MHE) is of significant importance, which can enrich the valley-related physics and emerging quantum states of matter. One exotic valley-related multiple Hall effect is the quantum anomalous valley Hall effect (QAVHE),[36–40] which possesses the interplay between valley and band topology and combines the valley index and quantum anomalous Hall effect (QAHE),[36] making it possible to realize high-performance quantum devices and thus raising an intensive interest in materials science. However, the realization of QAVHE[37] relies on the combination of SOC, band topology and magnetic ordering, which pose a great challenge for the research on potential high-performance valley-controllable quantum computational devices in 2D materials.

Motivated by these challenges, based on first-principles calculations with DFT+U approach and strained $k \cdot p$ model,[37] we have predicted single-layer (SL) $RuCl_2$ as an FV semiconductor, exhibiting intrinsic FM order and giant spontaneous valley polarization. Interestingly, we found that different electronic correlation strengths (U) and strains (ε)[41–44] make SL-$RuCl_2$ transition to different valley-controllable electronic states, including FV to half-valley[45] semimetal

[†]These authors contributed equally to this work and should be considered co-first authors.

[‡]Corresponding author. E-mail: ss_zhangchw@ujn.edu.cn

© 2023 Chinese Physical Society and IOP Publishing Ltd

(HVS) to QAVHE to HVS to FV state. These different electronic states are connected with valley-controllable sign-reversible Berry curvature. Remarkably, QAVHE phase, which combines both the features of QAHE and AVHE, can be realized due to band inversions of $d_{xy}/d_{x^2-y^2}$ and d_{z^2} orbitals at K/K' valleys. We further demonstrate that QAVHE phase of SL-$RuCl_2$ exists when electronic correlation strength (U) ranges from 2.19 eV to 2.29 eV. Even increasing U exceed this scope, take $U = 2.4$ eV, we can still observe QAVHE in the strain range of -2.3% and -1.1% by exerting biaxial compressive strain. Similar phase transition and QAVHE have also be reported in MBr_2,[43] $FeCl_2$, VSi_2P_4,[46] $VN_2X_2Y_2$ (X = group-III and Y = group-IV elements). These results broaden the avenue for low-dissipation electronics devices, highly promising for valleytronics and quantum computational devices.

2. Computational details

First-principles calculations with spin polarization within DFT are performed by the Vienna *ab initio* simulation package (VASP).[47–50] The generalized gradient approximation (GGA) with the Perdew–Burke–Ernzerhof (PBE) realization is used to describe the exchange–correlation effect.[51] The energy cutoff is chosen as 550 eV for expanding the wave functions and the total energy convergence criterion of 10^{-6} eV is adopted for static calculations. All the structural parameters are fully optimized until the force on each atom is converged to 0.01 eV/Å. A k-mesh of $17\times17\times1$ is used to sample the Brillouin zone and a vacuum layer about 20 Å to avoid the interactions between adjacent direction. To describe the on-site Coulomb interaction U terms of strong correlated Ru 4d electrons, we employed the GGA+U method.[52,53] Phonon spectrum is calculated by using $5\times5\times1$ supercell and $5\times5\times1$ q grid based on the density functional perturbation theory (DFPT) approach.[54] The Berry curvatures are calculated using the WANNIER90 package.[55] The edge states are calculated by using the iterative Green function method.[56]

3. Results and dicussion

In analogy to the TMDs, SL-$RuCl_2$ possess $P\bar{6}m2$ symmetry with a D_{3h} point group, which is composed of Cl–Ru–Cl sandwich layer, and each Ru atom has six nearest Cl neighbors, forming a triangular prism lattice, as shown in Fig. 1(a). Thus, the P in SL-$RuCl_2$ is broken. Figure 1(b) displays the optimized lattice constants of SL-$RuCl_2$ with the U values ranging from 0 eV to 3 eV. We can see that the calculated constant increases from 3.46 Å to 3.61 Å with U increasing from 0 eV to 3 eV. By calculating the phonon spectrum in Fig. 1(c), no imaginary frequency modes are observed, which demonstrates SL-$RuCl_2$ is dynamically stable. In addition, we calculated the elastic constants to check the mechanical stability of SL-$RuCl_2$. The elastic tensor C with the $P\bar{6}m2$ point-group symmetry for SL-$RuCl_2$ can be reduced to

$$C = \begin{pmatrix} C_{11} & C_{12} & 0 \\ C_{12} & C_{11} & 0 \\ 0 & 0 & (C_{11}-C_{12})/2 \end{pmatrix}. \quad (1)$$

The calculated results show that C_{11} and C_{12} are 34.14 GPa and 14.66 GPa, respectively. The calculated C_{ij} satisfy the Born criteria for mechanical stability,[57] $C_{11} > 0$ and $C_{11} - C_{12} > 0$, which confirms the mechanical stability of SL-$RuCl_2$.

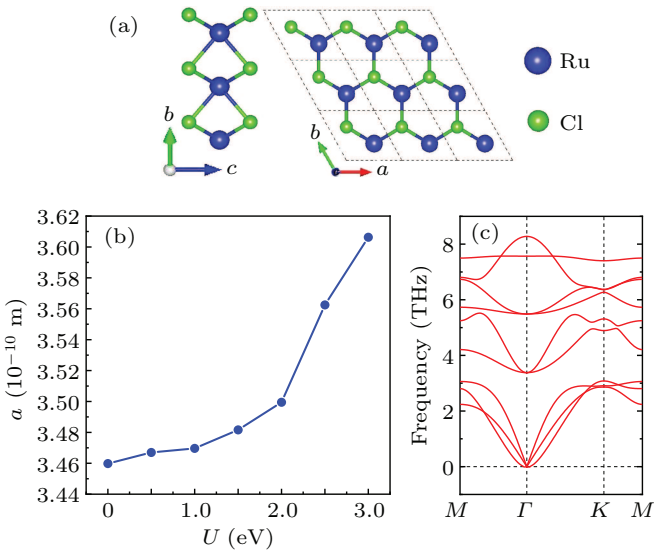


Fig. 1. (a) Side and top views of the crystal structure of SL-$RuCl_2$. (b) The optimized constants a as a function of U. (c) Phonon spectrum of SL-$RuCl_2$.

Next, we turn our attention to the magnetic properties of SL-$RuCl_2$. We consider three magnetic configurations, *i.e.*, nonmagnetic (NM) state, FM state, and antiferromagnetic (AFM) state, as shown in Fig. S1(a) in supporting information, The energy difference as a function of U is shown in Fig. S1(b). It is clear to see that SL-$RuCl_2$ always prefers FM state with U ranging from 0 eV to 3 eV, and the magnetic moment unit cell of FM phase is 4.0 μ_B per Ru atom. According to the Mermin–Wagner theorem,[58] the FM order is generally prohibited by thermal fluctuation if 2D FM systems are isotropic. However, the recent discoveries of FM ordering in 2D CrI_3[59] and $Cr_2Ge_2Te_6$,[60,61] with the presence of spin-wave excitation gap arising from magnetic anisotropy illustrate that FM ordering can exist at a finite temperature. Thus, to determine the magnetization easy axis of SL-$RuCl_2$, we calculate the magnetic anisotropy energy (MAE) under different U, as shown in Fig. S1(c). The MAE is defined as the energy difference between the systems with magnetization axis along in-plane (IP) and out-of-plane (OP) direction, namely $E_{MAE} = E_{100} - E_{001}$. We can find that SL-$RuCl_2$ prefers an OP-FM state when $U < 2.41$ eV, when $U > 2.41$ eV, it turns to IP-FM state.

For 2D FM materials, electronic correlations play an important role in its magnetic, valley and topological

properties.[62–65] Thus, we investigate the evolution of electronic band structures driven by electronic correlation (U) in SL-$RuCl_2$ and the representative electronic band structures without and with SOC are plotted in Fig. S2 and Fig. 2, respectively. Also, the evolution mechanism of the energy bandgap induced by different U is given in Fig. S3.

For a small U ($U = 0$ eV), SL-$RuCl_2$ exhibits an indirect gap semiconductor. The conduction band minimum (CBM) at K/K' valleys are mainly contributed by d_{z^2} orbital with the spin-down channel, and the spin-up d_{xz}/d_{yz} orbitals form the valence band maximum (VBM) (Fig. 2(a) and Fig. S2(a)). The opposite spin directions of VBM and CBM indicate SL-$RuCl_2$ possesses bipolar magnetic semiconductor (BMS) character. With increasing U before $U = 2.19$ eV, the global gap firstly increases and then decreases (Fig. S3(a)), and the orbitals of Ru-$d_{xy}/d_{x^2-y^2}$ move up relative to Ru-d_{xz} and Ru-d_{yz} orbitals gradually (Figs. 2(a)–2(d)). As shown in Fig. 2(d), on account of T and P broken, both the CBM and VBM belong to the spin-down channel, forming FV state with direct gap and the giant energy difference of band gap at K and K' valleys is 246.2 meV (Fig. S3(b)).

Around $U = 2.19$ eV, as shown in Fig. 2(e), the band gap at K' point gets closed, while still have a gap of 254.5 meV at K point. The gap closed at K' valley and opened at K valley indicating an HVS state. Here, taking SOC into account, HVS state indicates the Dirac cone shaped linear dispersion with intrinsically 100% spin valley polarization,[66] highly promising for charge and spin transport due to the mass-free electron mobility. Then we further increase U ($U > 2.19$ eV), the band gap at K' valley reopens and Ru-$d_{xy}/d_{x^2-y^2}$ bands continue to move up and thus exchange from VBM to CBM, the Ru-d_{z^2} component goes down and from CBM exchanges to VBM, correspondingly (Fig. 2(f)). Around $U = 2.29$ eV, another HVS states inevitably encountered, with the band gap closing at K valley, but the gap of about 247.1 meV at K' valley (Fig. 2(g)). Continuing increasing U, the band gap at K valley reopens and the CBM and VBM are apart from each other. From the perspective of orbital components, the Ru-d_{z^2} of CBM have been swapped with Ru-$d_{xy}/d_{x^2-y^2}$ orbitals of VBM at K valley. Hereafter SL-$RuCl_2$ returns to FV again. As can be seen from Fig. 2(h), the valley-polarization of SL-$RuCl_2$ distinctly occurs at the CBM and the giant energy difference of band gap at K/K' valleys is 240.3 meV (Fig. S3(b)). Thus, AVHE with an anomalous velocity $v_a \sim -(e/\hbar)E \times \Omega$ can be clearly observed (Fig. S4). When U is above 2.41 eV, SL-$RuCl_2$ turns to IP-FM state (Figs. 2(i) and 2(j)).

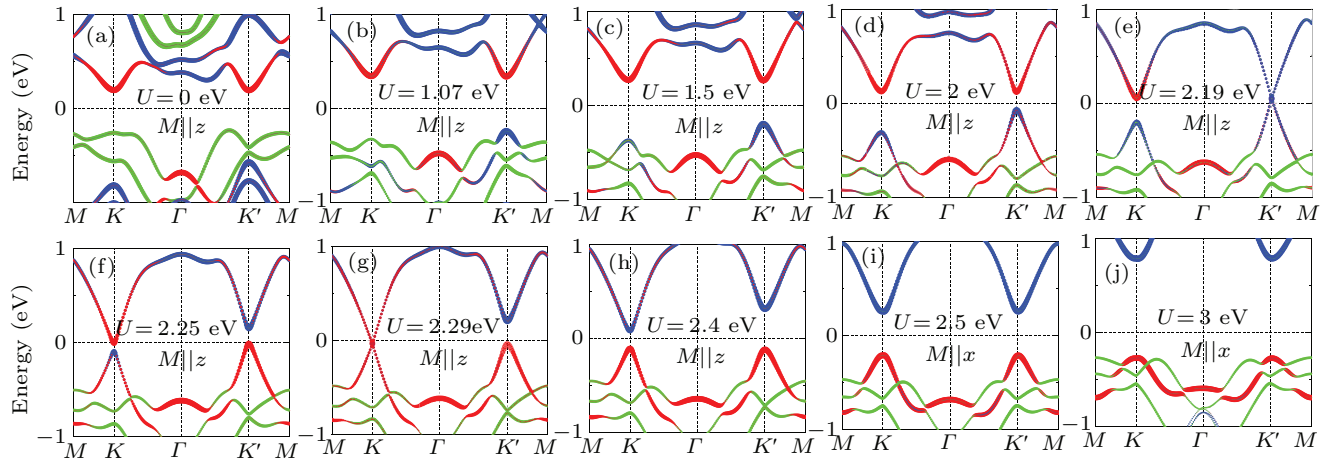


Fig. 2. Orbital-projected band structures of SL-$RuCl_2$ obtained from GGA+SOC+U (U varies from 0 eV to 3.0 eV). Blue circle represents components of Ru-d_{xy} and Ru-$d_{x^2-y^2}$ orbitals, red one is for component of Ru-d_{z^2} orbital, and the green one represents Ru-d_{xz} and Ru-d_{yz} orbitals.

Obviously, from the evolution of electronic band structures driven by U in SL-$RuCl_2$, one can see that when $U <$ 2.19 eV, VBM at K/K' valleys is primarily made up of Ru-$d_{xy}/d_{x^2-y^2}$ orbitals, while the energy degeneracy between two valleys is lifted and valley polarization apparently occurs at VBM (Fig. 2(d)). After the bandgap closing and reopening again at K and K' valleys, the Ru-$d_{xy}/d_{x^2-y^2}$ orbitals exchange completely from VBM to CBM, and the energy difference of CBM between K and K' valleys is larger than VBM contributed by Ru-d_{z^2} orbital (Fig. 2(h)).

With regard to the spontaneous valley-polarization of SL-$RuCl_2$, the underlying physical mechanisms can be attributed to the combining effect of magnetic exchange interaction and SOC. We take $U = 2$ eV as an example, the degeneracy between spin-up and spin-down channel is broken due to the existence of FM ordering. Since the VBM and CBM are both occupied by electrons with identical spin, we can ignore the interaction between spin-up and spin-down states. Thus, the SOC only involves the interaction of same spin channels, which can be approximately expressed by[33]

$$\hat{H}_{\mathrm{SOC}} = \lambda \hat{S}_z \left(\hat{L}_z \cos\theta + \frac{1}{2}\hat{L}_+ \mathrm{e}^{-\mathrm{i}\phi} \sin\theta + \frac{1}{2}\hat{L}_- \mathrm{e}^{+\mathrm{i}\phi} \sin\theta \right), \quad (2)$$

where $\hat{S}$ and $\hat{L}$ refers to the spin and orbital angular momentums, respectively. θ and ϕ define the polar angles of spin orientation. As MAE is in OP ($\theta = 0°$), equation (2) can be reduced to $\hat{H}_{\rm SOC} = \alpha \hat{L}_z$. In view of the orbitals' contribution and the wave vector symmetry at the K and K' points, the basis functions are chosen as $|\varphi_{\rm c}^{\tau}\rangle = |{\rm d}_{z^2}\rangle$ and $|\varphi_{\rm v}^{\tau}\rangle = \sqrt{1/2}\left(|{\rm d}_{x^2-y^2}\rangle + {\rm i}\tau|{\rm d}_{xy}\rangle\right)$, $\tau = \pm 1$ represents the valley index. v/c refers to the valence and conduction bands, respectively. According to the basic functions, the energy levels of the VBM and CBM at K' valley are given by $E_{\rm v}^{\tau} = \langle\varphi_{\rm v}^{\tau}|\hat{H}_{\rm SOC}|\varphi_{\rm v}^{\tau}\rangle$ and $E_{\rm c}^{\tau} = \langle\varphi_{\rm c}^{\tau}|\hat{H}_{\rm SOC}|\varphi_{\rm c}^{\tau}\rangle$, respectively. Accordingly, the valence (conduction) energy difference $\Delta E_{\rm v}$ ($\Delta E_{\rm c}$) at K/K' valleys can be expressed as[33,35]

$$\begin{aligned}\Delta E_{\rm v} &= E_{\rm v}^{-} - E_{\rm v}^{+} = {\rm i}\langle {\rm d}_{xy}|\hat{H}_{\rm SOC}|{\rm d}_{x^2-y^2}\rangle \\ &\quad - {\rm i}\langle {\rm d}_{x^2-y^2}|\hat{H}_{\rm SOC}|{\rm d}_{xy}\rangle, \end{aligned} \tag{3}$$

$$\Delta E_{\rm c} = E_{\rm c}^{-} - E_{\rm c}^{+} = 0. \tag{4}$$

From Eq. (3), we can obtain $\Delta E_{\rm v} = 4\alpha$. This indicates that valley polarization significantly occurs at VBM (Fig. 2(d)). After the completely swapping of Ru-$d_{xy}/d_{x^2-y^2}$ and Ru-d_{z^2} orbitals between VBM and CBM, as the case of $U = 2.4$ eV, we can infer that $\Delta E_{\rm c} = 4\alpha$, thus valley polarization evidently occurs at CBM (Fig. 2(h)). It is noteworthy that valley polarization can be reversed as the magnetization is reversed, which is confirmed by DFT results in Fig. S5. When the magnetization along the $-z$ direction, the spin and valley polarization of carriers is simultaneously switched. From a practical point of view, using intrinsic magnetism to generate valley polarization is more nonvolatile. Additionally, magnetism can be controlled in a fully electric manner, *e.g.*, by using current pulses through spin torques,[67] which is ideal for device applications.

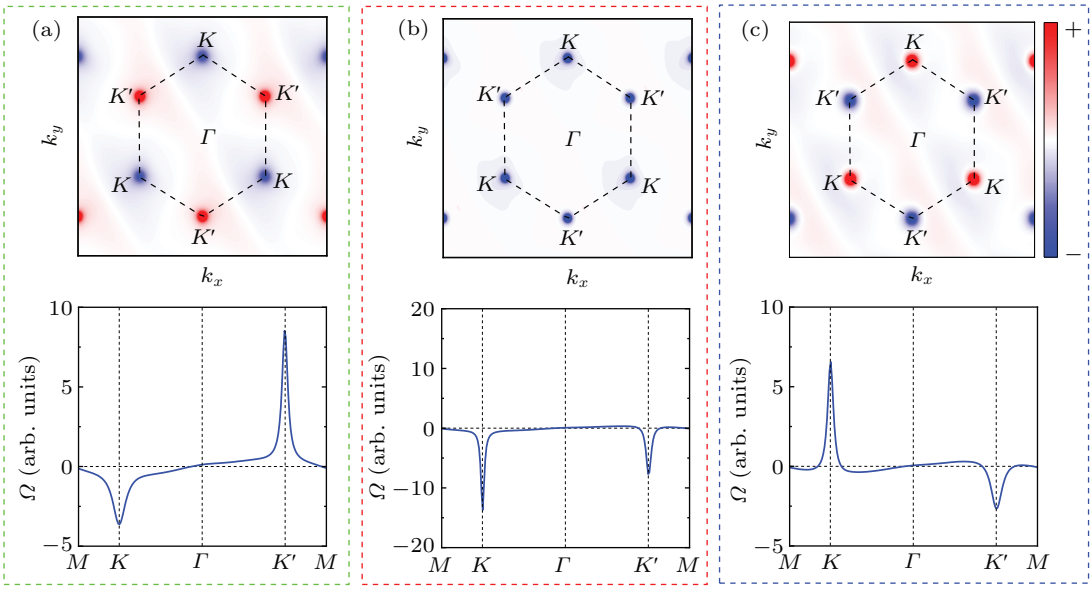


Fig. 3. Berry curvature of SL-$RuCl_2$ with $U = 2$ eV (a), 2.25 eV (b), 2.4 eV (c). The top planes are contour maps of Berry curvature in the whole 2D BZ, the bottom planes are Berry curvatures along the high-symmetry points.

Our most prominent finding is that SL-$RuCl_2$ is an exotic magneto-valley material, which can host several quantum phase diagrams driven by U starting from FV phase. Such an FV state is highly beneficial to generating, transporting, and manipulating spin currents in spin-valley spintronics. From the above discussion about the evolution of electronic band structures driven by U, we can observe that SL-$RuCl_2$ experienced two critical states, namely HVS state, appears at $U = 2.19$ eV and 2.29 eV, where the band gap closes at K' or K valley while another valley is still in semiconductor status. Along with the band gap reopening as U increases, the components of VBM and CBM at K/K' valleys also exchanged. This gap close–reopen scenario and interchanging of orbital compositions indicate a transition from trivial to nontrivial topological phase. This topological phase transition is correlated with valley-controllable sign-reversible Berry curvature as U variates. In order to investigate this phenomenon, the Berry curvature $\Omega(k)$ of SL-$RuCl_2$ is calculated based on the Kubo formula,[68] which could be performed with the following expression:

$$\Omega(k) = -\sum_{n}\sum_{n\neq n'} f(n)\frac{2\,{\rm Im}\langle\varphi_{nk}|v_x|\varphi_{n'k}\rangle\langle\varphi_{n'k}|v_y|\varphi_{nk}\rangle}{(E_n - E_{n'})^2}, \tag{5}$$

where n and n' are the band indexes, v_x and v_y are velocity operators in the x and y directions, respectively. $f(n)$ is the Fermi–Dirac distribution function. φ_{nk} and $\varphi_{n'k}$ are the periodic part of Bloch wave function with eigenvalue E_n and $E_{n'}$, respectively.

Figure 3 shows the Berry curvatures with $U = 2$ eV (a), 2.25 eV (b), 2.4 eV (c), respectively. As shown in Fig. 3(a), regarding FV state ($U = 2$ eV), a nonzero Berry curvature occurs around K/K' valleys with opposite signs and different magni-

tudes. When $U = 2.19$ eV, FV state experiences a topological phase transition into QAHVE state, bridged by an HVS state. For $U = 2.25$ eV, the sign of $\Omega(k)$ at K' valley flips (Fig. 3(b)). Further increasing $U = 2.29$ eV, K valley also experiences a topological phase transition, akin to the case of K' valley, resulting in the sign change of $\Omega(k)$ at K valley. With the increase of U, it transforms from HVS to another FV state. By comparing these two FV states, the sign of Berry curvature at K and K' valleys are quite opposite (Figs. 3(a) and 3(c)). Such dynamics of berry curvature $\Omega(k)$ is bound to influence valley-related anomalous transport phenomena, such as AHVE, valley Nernst effect, valley magneto-optical Kerr effect, and valley magneto-optical Faraday effect.[69]

It is remarkable that QAHVE phase in the range of $2.19\ \text{eV} < U < 2.29$ eV can be demonstrated by the calculated Berry curvatures in BZ space (Fig. 3(b)). Here, the Berry phase takes the same signs at K and K' valleys, but not the identical values. In this way, the edge spectrum calculated with WANNIER90 package shows a single gapless chiral state connecting the conduction and valence bands, consistent with an integer Chern number ($C = 1$), as shown in Fig. 4. Different from valley-polarized quantum anomalous Hall effect (VP-QAHE), the CBM, and VBM at K'/K valleys are all contributed by spin-down bands with full valley polarization (Fig. 4(a) and Fig. S5(b)). When the magnetization is reversed, the edge state changes to the other valley, with an opposite spin and chiral directions, as shown in Fig. 4(b), suggesting a very special behavior of the chiral-spin-valley locking for the obtained edge state. This novel quantum state can be detected by using the noncontact magneto-optical technique,[70] and thus highly promising for most practical applications in valleytronics.

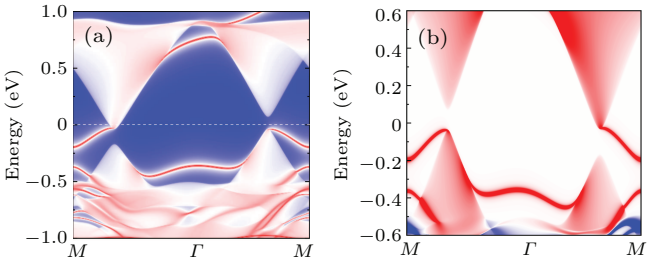


Fig. 4. (a) The calculated nontrivial chiral edge states for a semi-infinite SL-$RuCl_2$ with $U = 2.25$ eV. The 100% spin-polarized chiral state is locked with the valley index and spin direction. (b) The same as in panel (a), but the magnetization direction is along the $-z$ direction.

Yet for now, it is challenging to regulate the correlation effect (U), but we still hope that the various quantum phase diagram can be exhibited in practice. A crucial point is that the competition between kinetic and interaction energies could influence the strength of electronic correlation, which means we could exert epitaxial strain to manipulate the electronic and magnetic properties of 2D materials and thus probably achieve the same effect as changing U. Therefore, the biaxial strain is applied to the SL-$RuCl_2$. The strain strength is defined as $\varepsilon = (a - a_0)/a_0$, where a and a_0 are the lattice constants of the system with and without strain, respectively. Hence, the system of SL-$RuCl_2$ can be possibly tuned into FV, HVS, and QAVHE states, even though the electronic correlation strength U is larger than 2.19 eV. We use $U = 2.4$ eV as an example to explore the quantum phase transitions by exerting external biaxial strain. To confirm the FM ground states, the total energy difference between FM and AFM ordering by using rectangle supercell is calculated as a function of ε, as shown in Fig. S6(a). In considered strain range, the magnetic ground states are always the FM states, And the magnetic anisotropy of SL-$RuCl_2$ prefers the OP state under the considered range, as is shown in Fig. S6(b).

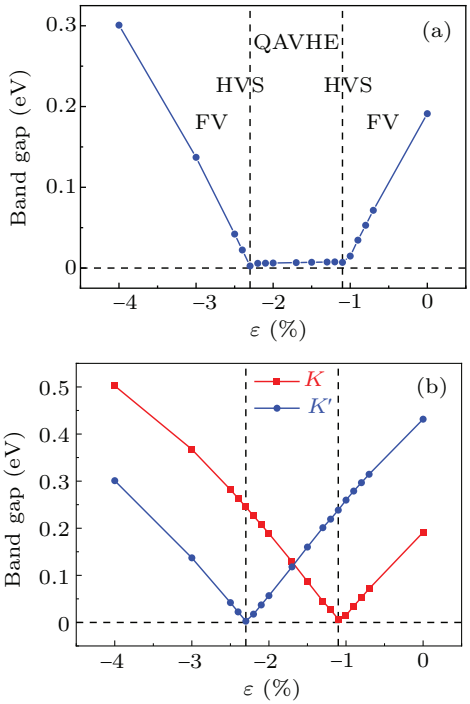


Fig. 5. (a) The global energy band gap as a function of ε ($0\% \sim -4\%$). (b) The energy band gaps for the K and K' valleys.

The energy band gap and orbital-projected band structures of SL-$RuCl_2$ under various types of biaxial strain are presented in Figs. 5 and 6, respectively. With increasing compressive biaxial strain, the gaps at two valleys decreases, when $\varepsilon = -1.1\%$, the band gap at K valley is closed, but it is still open at K' valley, transforming from FV to HVS state (Figs. 5(b) and 6(b)). Further increasing compressive strain until $\varepsilon = -2.3\%$, the gap at K valley reopens and closes gradually at K' valley, and the other HVS state can be achieved, as is shown in Fig. 6(d). Continuing increasing compressive biaxial strain, the band gap at K' valley will reopen and the system of SL-$RuCl_2$ will turn to the other FV state.

In the process of applying biaxial compressive strain, the system of SL-$RuCl_2$ also encounters two different critical states, i.e., HVS state, with the band gap closes at K and

K' valley, respectively. And the band gap reopening as compressive ε increases along with the swapping of Ru-$d_{xy}/d_{x^2-y^2}$ and Ru-d_{z^2} orbitals. This exotic transition probably suggests that QAVHE phases exist between the two HVS states. And this strain-induced phase transition mechanism for SL-$RuCl_2$ can be explained by constructing a $k \cdot p$ model.[35] In order to confirm QAVHE, we calculate the edge spectrum, as is shown in Fig. 7. We can clearly observe that a single edge band for connecting the bulk conduction and valence bands, which verifies its nontrivial topology and also indicates a very special behavior of the chiral-spin-valley locking. The QAVHE can also be observed between the two HVS states. With increasing biaxial compressive strain, SL-$RuCl_2$ can transform from FV to HVS to QAVHE to HVS to FV state.

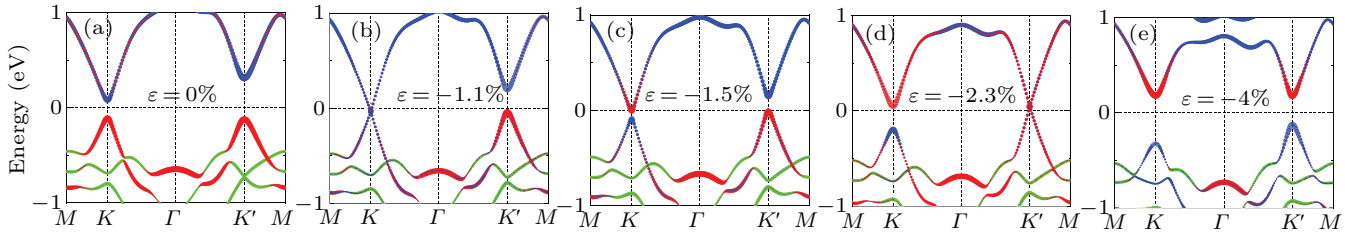


Fig. 6. Orbital-projected band structures of SL-$RuCl_2$ with SOC under different biaxial strains. Blue circle represents components of Ru-d_{xy} and Ru-$d_{x^2-y^2}$ orbitals, red one is for component of Ru-d_{z^2} orbital, and the green one represents Ru-d_{xz} and Ru-d_{yz} orbitals.

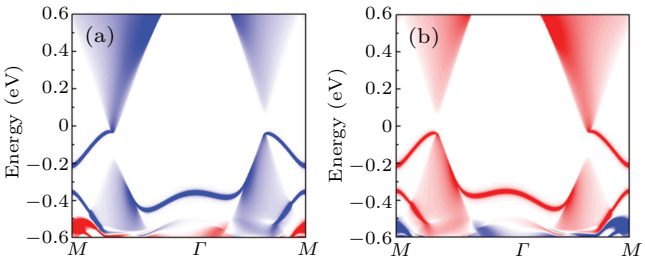


Fig. 7. (a) The calculated nontrivial chiral edge states for a semi-infinite SL-$RuCl_2$ with $\varepsilon = -1.5\%$. The 100% spin-polarized chiral state is locked with the valley index and spin direction. (b) The same as in panel (a), but the magnetization direction is along the $-z$ direction.

The valley-controllable sign-reversible Berry curvature is also related to the biaxial compressive strain, and we plot the Berry curvatures at some representative ε values in Fig. 8. For a small compressive strain ($\varepsilon = -0.7\%$), as shown in Fig. 8(a), we find that a nonzero Berry curvature occurs around K/K' valleys with opposite signs and different magnitudes, consistent with the FV state. Under the strain of -1.1%, the sign of Berry curvature at K valley firstly flips, and then the Berry curvature at K' valley change sign at about $\varepsilon = -2.3\%$. These topological phase transitions are also related to the band inversion of $d_{xy}/d_{x^2-y^2}$ and d_{z^2} orbitals, being similar to varied U. Our understanding of the change of sign for the berry curvature at two valleys is that the opposite and half quantized Hall conductivity $e^2/2h$ and $-e^2/2h$, respectively. The phase transition at two valleys happens at two different critical on-site Coulomb interactions: When $U < 2.19$ eV, $C = 1/2 - 1/2 = 0$; when $U > 2.29$ eV, $C = -1/2 + 1/2 = 0$, while in the case of 2.19 eV $< U <$ 2.29 eV, Berry curvature at one of the two valleys changes its sign and leads a total Chern number as $1/2 + 1/2 = 1$.

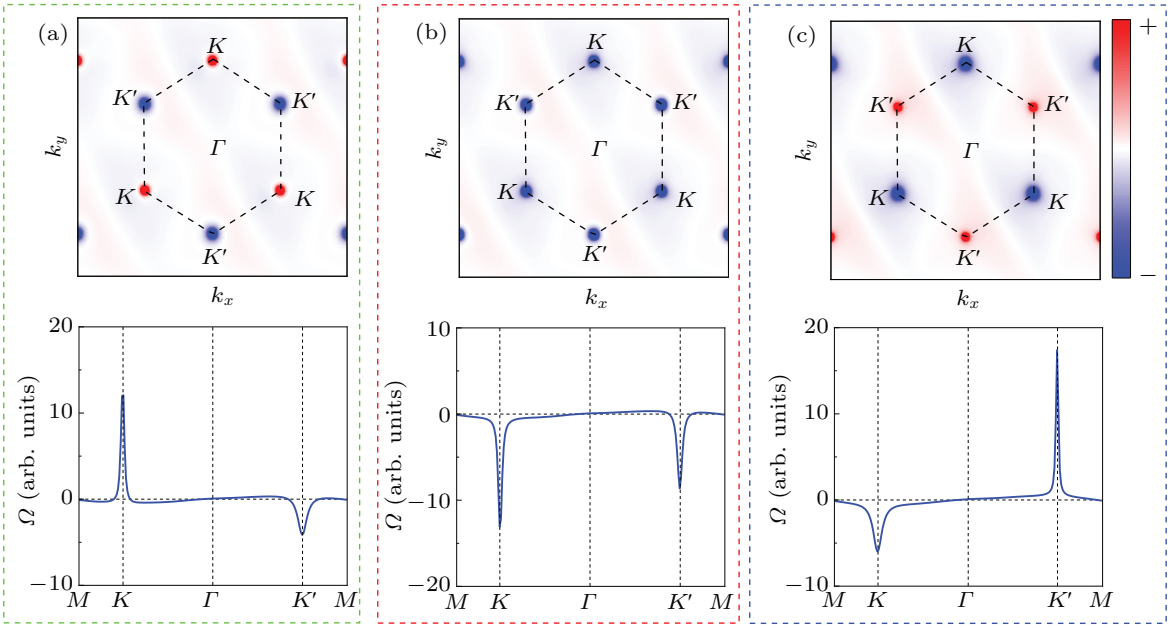


Fig. 8. Berry curvature of SL-$RuCl_2$ with $\varepsilon = -0.7\%$ (a), -1.5% (b), -2.5% (c) at $U = 2.4$ eV. The top planes are contour maps of Berry curvature in the whole 2D BZ, the bottom planes are Berry curvatures along the high-symmetry points.

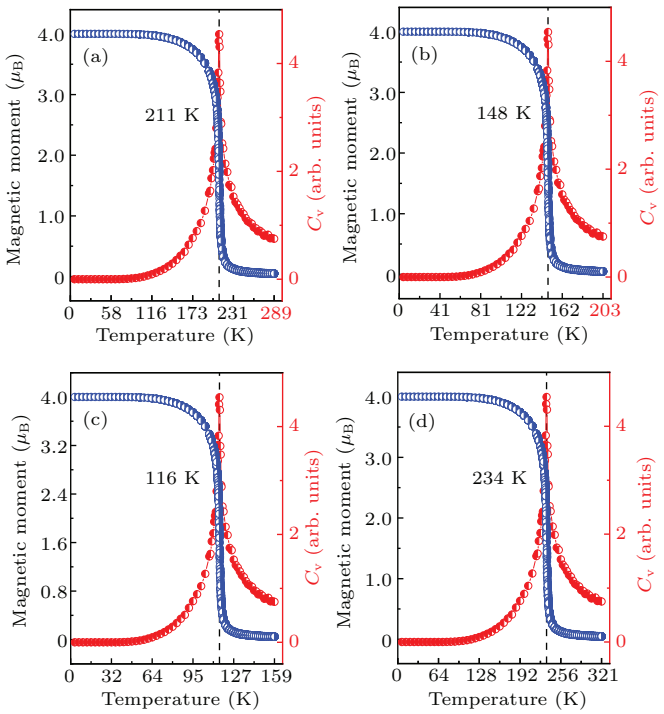


Fig. 9. The average magnetic moment and specific heat as a function of temperature with $U = 2$ eV (a), 2.25 eV (b), and $\varepsilon = 0\%$ (c), -4% (d) at $U = 2.4$ eV.

Both electronic correlation effects and compressive strain can effectively tune the strength of FM interaction, which can produce important effects on Curie temperature T_c of SL-$RuCl_2$. The T_c is estimated at representative U (2 eV, 2.25 eV, and 2.4 eV) and ε (0% and -4%) values with the Wolf algorithm based on the Heisenberg model, which can be expressed as[71]

$$H = -\sum_{i,j} J_{i,j} S_i S_j - \sum_i A_i S_i^z S_i^z, \tag{6}$$

where $J_{i,j}$ represents the exchange parameters of the nearest neighbor, which could be calculated according to the energy difference between FM and AFM configurations. Here S_i/S_j is the spin vector on each Ru, A_i is the anisotropy energy parameter per magnetic atom, and S_i^z is the z component of the spin vector. As the distance between Ru atoms and its second nearest neighboring Ru is more than 6.0 Å, which is along enough to be ignored, only the nearest J is taken into account.[46]

$$E_{FM} = E_0 - 6J|S|^2 - A|S_Z|^2, \tag{7}$$

$$E_{AFM} = E_0 + 2J|S|^2 - A|S_Z|^2. \tag{8}$$

Thus

$$J = \frac{E_{AFM} - E_{FM}}{8|S|^2}. \tag{9}$$

On comparing with the energy results from first-principles calculations, the obtained model parameters are found to be $J = 4.97$ meV and $A = 117.5$ μeV for $U = 2$ eV, $J = 3.50$ meV and $A = 62.3$ μeV for $U = 2.25$ eV, $J = 2.73$ meV and $A = 0.188$ μeV for $U = 2.4$ eV at $\varepsilon = 0\%$, $J = 5.53$ meV and $A = 158.9$ μeV for $U = 2.4$ eV at $\varepsilon = -4\%$. To make the FM-paramagnetic transition clearer, we calculate the heat capacity (C_v) as follows:

$$C_v = \frac{\Delta E_T}{\Delta T}, \tag{10}$$

Here, ΔE_T is the change of the total energy as the temperature increases from T to $T + \Delta T$. The Monte Carlo simulation is then performed to estimate the transition point of the ferromagnetism, and the results shown in Fig. 9. The estimated T_c is about 211 K for $U = 2$ eV, 148 K for $U = 2.25$ eV, 116 K, and 234 K for $U = 2$ eV at $\varepsilon = 0\%$ and -4%. Thus, it is very key for estimating T_c to use reasonable U. And it is found that the compressive strain can improve T_c.

4. Conclusions

To summarize, based on first-principles calculations with DFT+U approach and a $k \cdot p$ model, we found that valley-controlled quantum phase transitions can be driven by electronic correlation and compressive biaxial strain from FV to HVS to QAVHE to HVS to FV phase in SL-$RuCl_2$. Remarkably, QAVHE and chiral spin-valley, which is induced by sign-reversible Berry curvature or band inversion between $d_{xy}/d_{x^2-y^2}$ and d_{z^2} orbitals, can achieve complete spin and valley polarizations for low-dissipation electronics devices. We also find that this electron valley-polarization can be switched by reversing the magnetization direction, providing a new route of magnetic control of valley degree of freedom. Therefore, our findings not only enrich the research on QAVHE, but also broaden the horizon for the spintronics, valleytronics, and topological nanoelectronics applications.

Acknowledgements

Project supported by the Taishan Scholar Program of Shandong Province, China (Grant No. ts20190939), the Independent Cultivation Program of Innovation Team of Jinan City (Grant No. 2021GXRC043), and the National Natural Science Founation of China (Grant No. 52173283).

References

[1] Schaibley J R, Yu H Y, Clark G, Rivera P, Ross J S, Seyler K L, Yao W and Xu X D 2016 *Nat. Rev. Mater.* **1** 16055
[2] Wolf S A, Awschalom D D, Buhrman R A, Daughton J M, Molnar S von, Roukes M L, Chtchelkanova A Y and Treger D M 2001 *Science* **294** 1488
[3] Xiao D, Yao W and Niu Q 2007 *Phys. Rev. Lett.* **99** 236809
[4] Han Y T, Ji W X, Wang P J, Li P and Zhang C W 2023 *Nanoscale* **15** 6830
[5] Xiao D, Liu G B, Feng W, Xu X and Yao W 2012 *Phys. Rev. Lett.* **108** 196802
[6] Liu Y, Gao Y, Zhang S, He J, Yu J and Liu Z 2019 *Nano Res.* **12** 2695
[7] Splendiani A, Sun L, Zhang Y, Li T, Kim J, Chim C Y, Galli G and Wang F 2010 *Nano Lett.* **10** 1271
[8] Eftekhari A and Mater 2017 *J. Chem. A* **5** 18299

[9] Radisavljevic B, Radenovic A, Brivio J, Giacometti V and Kis A 2011 *Nat. Nanotechnol.* **6** 147
[10] Li S S, Ji W X, Hu S J, Zhang C W and Yan S S 2017 *Appl. Mater. Inter.* **9** 41443
[11] Wang Y P, Ji W X, Zhang C W, Li P, Zhang S F, Wang P J, Li S S and Yan S S 2017 *Appl. Phys. Lett.* **110** 213101
[12] Pan H, Li Z, Liu C C, Zhu G, Qiao Z and Yao Y 2014 *Phys. Rev. Lett.* **112** 106802
[13] Ding J, Qiao Z, Feng W, Yao Y and Niu Q 2011 *Phys. Rev. B* **84** 195444
[14] Wu S, Ross J S, Liu G B, Aivazian G, Jones A, Fei Z, Zhu W, Xiao D, Yao W, Cobden D and Xu X D 2013 *Nat. Phys.* **9** 149
[15] Zeng H, Dai J, Yao W, Xiao D and Cui X 2012 *Nat. Nanotechnol.* **7** 490
[16] Ye Z L, Sun D Z and Heinz T F 2017 *Nat. Phys.* **13** 26
[17] Mak K F, He K, Shan J and Heinz T F 2012 *Nat. Nanotechnol.* **7** 494
[18] Cheng Y C, Zhang Q Y and Schwingenschlögl U 2014 *Phys. Rev. B* **89** 155429
[19] Peng R, Ma Y, Zhang S, Huang B and Dai Y 2018 *J. Phys. Chem. Lett.* **9** 3612
[20] Singh N and Schwingenschlogl U 2017 *Adv. Mater.* **29** 1600970
[21] Xu L, Yang M, Shen L, Zhou J, Zhu T and Feng Y P 2018 *Phys. Rev. B* **97** 041405
[22] Wang B J, Sun Y Y, Chen J, Ju W W, An Y P and Gong S J 2021 *J. Mater. Chem. C* **9** 3562
[23] Seyler K L, Zhong D, Huang D, Linpeng X, Wilson N P, Taniguchi T, Watanabe K, Yao W, Xiao D, McGuire M A, Fu K C and X Xu 2018 *Nano Lett.* **18** 3823
[24] Cai T, Yang S A, Li X, Zhang F, Shi J, Yao W and Niu Q 2013 *Phys. Rev. B* **88** 115140
[25] MacNeill D, Heikes C, Mak K F, Anderson Z, Kormanyos A, Zolyomi V, Park J and Ralph D C 2015 *Phys. Rev. Lett.* **114** 037401
[26] Zhang X X, Cao T, Lu Z, Lin Y C, Wang Y, Li Z, Hone J C, Robinson J A, Smirnov D, Louie S G and Heinz T F 2017 *Nat. Nanotech.* **12** 883
[27] Srivastava A, Sidler M, Allain A V, Lembke D S, Kis S and Imamoğlu A 2015 *Nat. Phys.* **11** 141
[28] Tong W Y, Gong S J, Wan X and Duan C G 2016 *Nat. Commun.* **7** 13612
[29] Luo C, Peng X, Qu J and Zhong J 2020 *Phys. Rev. B* **101** 245416
[30] Zhao P, Ma Y, Lei C, Wang H, Huang B and Dai Y 2019 *Appl. Phys. Lett.* **115** 261605
[31] Jiang P, Kang L, Li Y L, Zheng X, Zeng Z and Sanvito S 2021 *Phys. Rev. B* **104** 035430
[32] Guo S D, Zhu J X, Mu W Q and Liu B G 2021 *Phys. Rev. B* **104** 224428
[33] Sheng K, Chen Q, Yuan H K and Wang Z Y 2022 *Phys. Rev. B* **105** 075304
[34] Li S, He J, Grajciar L and Nachtigall P 2021 *J. Mater. Chem. C* **9** 11132
[35] Cui Q, Zhu Y, Liang J, Cui P and Yang H 2021 *Phys. Rev. B* **103** 085421
[36] Zhou T, Zhang J, Jiang H, Žutić I and Yang Z 2018 *npj Quantum Mater.* **3** 39
[37] Huan H, Xue Y, Zhao B, Gao G, Bao H and Yang Z 2021 *Phys. Rev. B* **104** 165427
[38] Hu C S, Wu Y J, Liu Y S, Fu S, Cui X N, Wang Y H and Zhang C W 2022 *Chin. Phys. B* **32** 037306
[39] Liu Y S, Sun H, Hu C S, Wu Y J and Zhang C W 2022 *Chin. Phys. B* **32** 027101
[40] Zhang S J, Zhang C W, Zhang S F, Ji W X, Li P, Wang P J, Li S S and Yan S S 2017 *Phys. Rev. B* **96** 205433
[41] Guo S D, Mu W Q and Liu B G 2022 *2D Mater.* **9** 035011
[42] Zhang D, Li A, Chen X, Zhou W and Ouyang F 2022 *Phys. Rev. B* **105** 085408
[43] Sun H, Li S S, Ji W X and Zhang C W 2022 *Phys. Rev. B* **105** 195112
[44] Huan H, Xue Y, Zhao B, Guo G, Bao H and Yang Z 2021 *Phys. Rev. B* **104** 165427
[45] Zhang M H, Zhang C W, Wang P J and Li S S 2018 *Nanoscale* **10** 20226
[46] Li S, Wang Q, Zhang C, Guo P and Yang S A 2021 *Phys. Rev. B* **104** 085149
[47] Kresse G 1995 *Journal of Non-Crystalline Solids* **192–193** 222
[48] Kresse G and Furthmüller J 1996 *Comput. Mater. Sci.* **6** 15
[49] Kresse G and Joubert D 1999 *Phys. Rev. B* **59** 1758
[50] Zhang L, Zhang S F, Ji W X, Zhang C W, Li P, Wang P J, Li S S and Yan S S 2018 *Nanoscale* **10** 20748
[51] Perdew J P, Burke K and Ernzerhof M 1996 *Phys. Rev. Lett.* **77** 3865
[52] Liechtenstein A I, Anisimov V V and Zaanen J 1995 *Phys. Rev. B* **52** R5467
[53] Zhang Y, Lin L, Moreo A and Dagotto E 2022 *Phys. Rev. B* **105** 085107
[54] Togo A and Tanaka I 2015 *Scr. Mater.* **108** 1
[55] Mostofi A A, Yates J R, Pizzi G, Lee Y S, Souza I, Vanderbilt D and Marzari N 2014 *Comput. Phys. Commun.* **185** 2309
[56] López Sancho M P, López Sancho J M and Rubio J 1984 *J. Phys. F* **14** 1205
[57] Cadelano E and Colombo L 2012 *Phys. Rev. B* **85** 245434
[58] Mermin N D and Wagner H 1966 *Phys. Rev. Lett.* **17** 1133
[59] Huang B, Clark K, Navarromoratalla E, Klein D R, Cheng R, Seyler K L, Zhong D, Schmidgall E, Mcguire M A and Cobden D H 2017 *Nature* **546** 270
[60] Gong C, Li L, Li Z L, Ji H W, Stern A, Xia Y, Cao T, Bao W, Wang C, Wang Y, Qiu Z Q, Cava R J, Louie S G, Xia J and Zhang X 2017 *Nature* **546** 265
[61] Liu W R, Dong X J, Lv Y Z, Ji W X, Cao Q, Wang P J, Li F and Zhang C W 2022 *Nanoscale* **14** 3632
[62] Xiang H J and Whangbo M H 2007 *Phys. Rev. B* **75** 052407
[63] Gray A X, Jeong J, Aetukuri N P, Granitzka P, Chen Z, Kukreja R, Highley D, Chase T, Reid A H, Ohldag H, Marcus M A, Scholl A, Young A T, Doran A, Jenkins C A, Shafer P, Arenholz E, Samant M G, Parkin S S P and Dürr H A 2016 *Phys. Rev. Lett.* **116** 116403
[64] Sorella S, Seki K, Brovko O O, Shirakawa T, Miyakoshi S, Yunoki S and Tosatti E 2018 *Phys. Rev. Lett.* **121** 066402
[65] Leonov I, Skornyakov S L, Anisimov V I and Vollhardt D 2015 *Phys. Rev. Lett.* **115** 106402
[66] Hu H, Tong W Y, Shen Y H, Wan X and Duan C G 2020 *npj Comput. Mater.* **6** 129
[67] Ma Y T, Wan C H, Wang X, Yang W L, Guo C Y, Fang C, . Zhao M K, Dong J, Zhang Y and Han X F 2020 *Phys. Rev. B* **101** 134417
[68] Thouless D J, Kohmoto M, Nightingale M P and Nijs M 1982 *Phys. Rev. Lett.* **49** 405
[69] Zhou X, Zhang R W, Zhang Z, Feng W, Mokrousov Y and Yao Y 2021 *npj Comput. Mater.* **7** 160
[70] Pan H, Li X, Jiang H, Yao Y and Yang S A 2015 *Phys. Rev. B* **91** 045404
[71] Zhang M H, Chen X L, Ji W X, Wang P J, Min-Yuan M Y and Zhang C W 2020 *Appl. Phys. Lett.* **116** 172105